High Temperature Corrosion of Materials (2024) 101:225–249
https://doi.org/10.1007/s11085-023-10213-y

ORIGINAL PAPER

The Effect of Milling Time and Hot-Pressing on the Structural Properties and Wear Behavior of CoCrFeMnNi High-Entropy Alloys Fabricated by Mechanical Alloying

Caner Bulut[1] · Fatih Yıldız[2] · Temel Varol[3,4] · Serhatcan Berk Akçay[3] · Tevfik Oğuzhan Ergüder[2]

Received: 21 August 2023 / Revised: 8 November 2023 / Accepted: 20 November 2023 /
Published online: 12 December 2023
© The Author(s), under exclusive licence to Springer Science+Business Media, LLC, part of Springer Nature 2023

Abstract

In this work, CoCrFeMnNi high-entropy alloys (HEAs) were fabricated by mechanical alloying and hot-pressing-assisted powder metallurgy method. For HEA powders, the effect of milling time on the morphology, particle size, crystallite structure and oxidation resistance of the HEA particles was studied. For sintered HEAs, effects of milling time and hot-pressing on the microstructure evolution, density, hardness, friction coefficient, wear rate and surface roughness of CoCrFeMnNi HEAs were investigated. Milling the particles for 5 h resulted in further cold welding of the initial particles and the formation of many coarse and cold-welded particles. The particle-size distribution obtained after 5 h of milling was single peaked and had a relatively narrow distribution range. An increase in oxidation resistance with increasing milling time was observed due to the embedding of hard and highly oxidation-resistant particles such as Co, Cr and Ni into ductile Fe particles. The CoCrFeMnNi alloy produced with 5 h of milling and at 650 MPa pressure had the highest relative density with 86.29%, while the sample fabricated with 0.5 h of milling and 550 MPa pressure showed the lowest relative density with 77.34%. The lowest wear rate was obtained in the sample produced with 5 h of milling and at 650 MPa. At the same time, the lowest average coefficient of friction was obtained as approximately 0.28 for the sample produced under these conditions.

Keywords High-entropy alloys · CoCrFeMnNi alloy · Mechanical alloying · Hot-pressing · Powder metallurgy · Wear

Extended author information available on the last page of the article

Introduction

Conventional alloys are generally formed from one or two main elements and other alloying elements added in small amounts to improve the properties of the alloy [1, 2]. In the 2000s, Yeh et al. [2, 3] and Cantor et al. [4] independently proposed a new type of multicomponent alloy called high-entropy alloy (HEA). HEAs are structures formed as solid melts in which at least five elements have a composition in equal or nearly equal atomic ratios [5–8]. In general, HEAs contain 5–13 major elements, and the concentration of each element varies between 5 and 35% [9, 10]. The HEAs have good thermal stability, good workability, corrosion resistance, high strength, and crystalline structure at both high and low temperatures [11–13]. In these types of alloys, the close ratio of many elements in the alloy leads to a high mixing entropy. Therefore, they tend to complicate the formation of intermetallic phases and instead form irregular or partially ordered body-centered cubic (BCC), face-centered cubic (FCC) or a combination of the two (BCC + FCC) and hexagonal close-packed (HCP) structures [10, 12, 14–16].

HEA are usually produced by conventional metallurgical methods such as arc melting or induction melting [17]. However, in the case of arc melting and casting, segregation and dendritic microstructure [18, 19] that occur during solidification can significantly affect mechanical properties and require secondary treatment [1, 17, 20]. Moreover, metals at low melting temperatures in the HEA structure evaporate during production by liquid-phase methods [21], and in this case, the expected composition cannot be achieved. The mechanical alloying method, which is preferred in the production of HEAs and has an important share, is realized in the form of solid-state structure. Mechanical alloying is an unbalanced process that allows the milling of different forms and types of elemental powders in high-energy mills by storing mechanical energy. This process is widely used for the synthesis of nanomaterials, alloy and composite powders with good homogeneity [10, 22–26]. Mechanical alloying also promotes the formation of single-phase structures due to the grain refinement of the elements and the expansion of mutual solid solubility [10, 27].

CoCrFeMnNi HEA is widely studied for its superior fracture toughness and high strength at both room and cryogenic temperatures and is considered one of the promising HEA types for industrial applications [28–30]. Li et al. [31] reported that their non-equimolar CoCrFeMnNi HEAs exhibited a combination of high strength and ductility. Nagarjuna et al. [32] investigated the mechanical properties and wear resistance of the structure by producing equimolar CoCrFeMnNi alloy at different times (5, 10, 30 and 60 min) and at 800 rpm by mechanical alloying process. They observed that as the milling time increased, the alloy powder shapes changed and the mechanical properties increased. They also reported that the wear rate decreased with time. Yim et al. [33] also reported that particle size and particle size distribution were effective on the compaction density of CoCrFeMnNi alloy powders, and that the relative density of small particle powders was lower than larger particles. CoCrFeMnNi HEA produced by mechanical alloying was reported to exhibit predominantly FCC phase and good

mechanical properties [34–36]. Joo et al. [37] reported that mechanical alloying time and sintering temperature affect the microstructure and mechanical properties of CoCrFeMnNi alloy. At 60 min mechanical alloying and 900 °C spark plasma sintering, they observed that fine-grained microstructure was obtained and the structure exhibited FCC phase.

When the literature is examined, it has been observed that the mechanical and wear properties of CoCrFeMnNi high-entropy alloys obtained under different temperatures and pressures have not been examined as a whole and no comparison has been made in these parameters. In this study, to produce CoCrFeMnNi HEA with powder metallurgy technology, the powders forming the alloy were mechanically alloyed for grain refinement and homogenization at different milling times. In addition, samples were produced by applying hot-pressing in two separate groups in order to create a high density stable solid solution composition from the milled powders. The phase evolution, microstructure and wear behavior of the produced samples were systematically investigated. Moreover, it is aimed to determine the optimum milling time and hot-pressing parameters for the HEA.

Experimental Procedures

Fabrication of HEA Powders

In this study, high-purity Co, Cr, Fe, Mn, Ni (> 99 wt%) powders from Nanokar Chemicals Industry and Trade Ltd. Co. (Turkey) were used to produce the CoCrFeMnNi high-entropy alloy. The initial average particle size information of Co, Cr, Fe, Mn, Ni powders from the supplier was approximately < 100 μm. As-received powders were milled by adding equal weight of each component. Mechanical alloying process was carried out at the durations of 0.5–1–3–5 h. Retsch PM 100 planetary ball milling was used to mechanical alloying processes. The milling speed, ball to powder ratio (BPR) and process control agent (PCA) are selected as 400 rpm, 10:1 and 2 wt%, respectively. WC jar and balls with a 10 mm diameter were used as milling media. Methanol was used as PCA in all mechanical alloying processes. Methanol was only added into the jar at the beginning of the process. In this context, the production parameters of the HEA powders produced together with the test codes are given in Table 1.

Table 1 Production parameters of HEA powders

Sample code	Milling speed (rpm)	BPR	PCA (%wt.)	Milling time (h)
HEA-P-1	400	10:1	2	0.5
HEA-P-2				1
HEA-P-3				3
HEA-P-4				5

Fabrication of HEA Bulk Materials

After the mechanical alloying process, CoCrFeMnNi HEA alloy powders were fabricated by hot-pressing technique to obtain CoCrFeMnNi HEA compact materials. Powder metallurgy process parameters are given in Table 2. For each sample production, 5 g of powder was filled into the mold cavity, which measured 12.7 mm, and then intensified by temperature and pressure. For the densification of HEA powders, 550 and 650 MPa pressures were used in hot-pressing at 600 °C. The graphite lubricant was used to reduce friction on the mold to improve densification capability. Afterward, all samples were subjected to sintering process in a vacuum atmosphere in the oven with a waiting time of 2 h at 1000 °C. Surface roughness values and wear volumes of the samples were assessed through the utilization of the Bruker Contour GT 3D optical profilometer.

Structural Characterization

Particle size distribution experiments were performed using the Malvern-Mastersizer Hydro 2000 instrument. XRD measurements for powder and bulk samples were made with GNR Explorer X-ray diffraction device and Cu-Kα anode X-ray source with a wavelength of 1.5405°A. Measurements were obtained at 0.05° steps per second with a symmetrical scan configuration in the 20°–90° range. The XRD data were analyzed with the JCPDS (Joint Committee on Powder Diffraction Standards) cards in the Match software, and the phase contents were determined and verified with the literature data. Scanning electron microscopy (SEM) and energy dispersive spectrometry (EDS) analysis were performed with a Quanta-FEG 250 and ZEISS Sigma 300 instruments to determine the microstructure images and quantitative chemical analysis of the elements. Thermogravimetric analysis was performed using the PerkinElmer TGA 4000 thermogravimetric analyzer. Thermogravimetric analyses were carried out using 20 ℃/min heating rate. The surfaces of the samples were sanded up to 1200 grit and polished with alumina suspension. For the microstructure examinations of the produced samples, they were chemically etched in a 1:1:1 ratio of HCl, HNO_3, and distilled water solution. The surface morphologies of the experimental samples were investigated using Carl Zeiss Scope A1 optical microscope and SEM. The average roughness (Ra) values of the produced bulk sample surfaces were determined by the images taken from five different parts of the sample surface using a 3D profilometer device. Densities were determined in accordance with the Archimedes principle. Hardness tests were carried out with Brinell hardness measuring device using 2.5-mm-diameter steel ball at a load of 31.25 kgf.

Wear Tests

In order to examine the effects of hot-pressing pressure and milling time on the wear resistance of CoCrFeMnNi HEAs, wear tests were carried out with a

Table 2 Powder metallurgy process parameters

Sample code	Pressure (MPa)	Milling time (h)	Hot-pressing temperature (°C)	Hot-pressing time (h)	Sintering temperature (°C)	Sintering time (h)
HEA-HP-1	550	0.5	600	2	1000	2
HEA-HP-2	550	1				
HEA-HP-3	550	3				
HEA-HP-4	550	5				
HEA-HP-5	650	0.5				
HEA-HP-6	650	1				
HEA-HP-7	650	3				
HEA-HP-8	650	5				

Table 3 Wear test parameters

Test parameters	Values
Test type	Reciprocating
Wear stroke, mm	4
Velocity, mm/s	8
Normal load, N	5
Time, s	2100
Ball type	Al_2O_3
Temperature, °C	Room temperature (20 ± 2)
Ambient	Dry conditions

Bruker-UMT tribometer tester. The parameters used in the wear tests are given in Table 3.

Bruker Contour GT 3D profilometer was used to determine the wear volumes of the samples after the wear tests. The wear volumes were obtained by multiplying the cross-sectional area of the wear trace, which was determined by taking an average of ten measurements from each wear trace, by the Vision64 software, by the length of each trace. The wear tests were repeated twice for each sample and the wear rates were calculated with the following formula:

$$\text{Wear rate}\left(\frac{\text{mm}^3}{\text{Nm}}\right) = \frac{\text{Wear Volume } \left(\text{mm}^3\right)}{\text{Wear distance(m). Normal load (N)}} \quad (1)$$

Results and Discussion

Powder Properties and Mechanical Alloying Process

Initial morphology images of the particles (Fe, Cr, Ni, Co, Mn) used for the fabrication of HEAs are shown in Fig. 1a–e. As can be seen in Fig. 1a, the initial morphology of the Fe particles was relatively spherical. Figure 1a shows that there are Fe powders ranging in size from 10 to 80 µm in the powder mass. The morphology of the Cr particles was irregular (Fig. 1b). According to Fig. 1b, the powder mass contains Cr powders with particles sizes ranging from 5 to 30 µm. SEM image of the Ni particles is shown in Fig. 1c. As can be seen in Fig. 1c, Ni particles have dendrite-like morphology, and it has a variable particle size range between 5 and 90 µm. As seen in SEM image (Fig. 1c), the Ni particles seems fine particles, but according to particle size distribution graph (Fig. 2), there are some differences. This can be explained with the dendritic morphology of Ni. In dendritic morphology, there is a stem and branches of different lengths attached to the stem. This leads to a wide particle size distribution in particle size analysis because the particle is likely to have different dimensions along the axis of length, width, and thickness. In

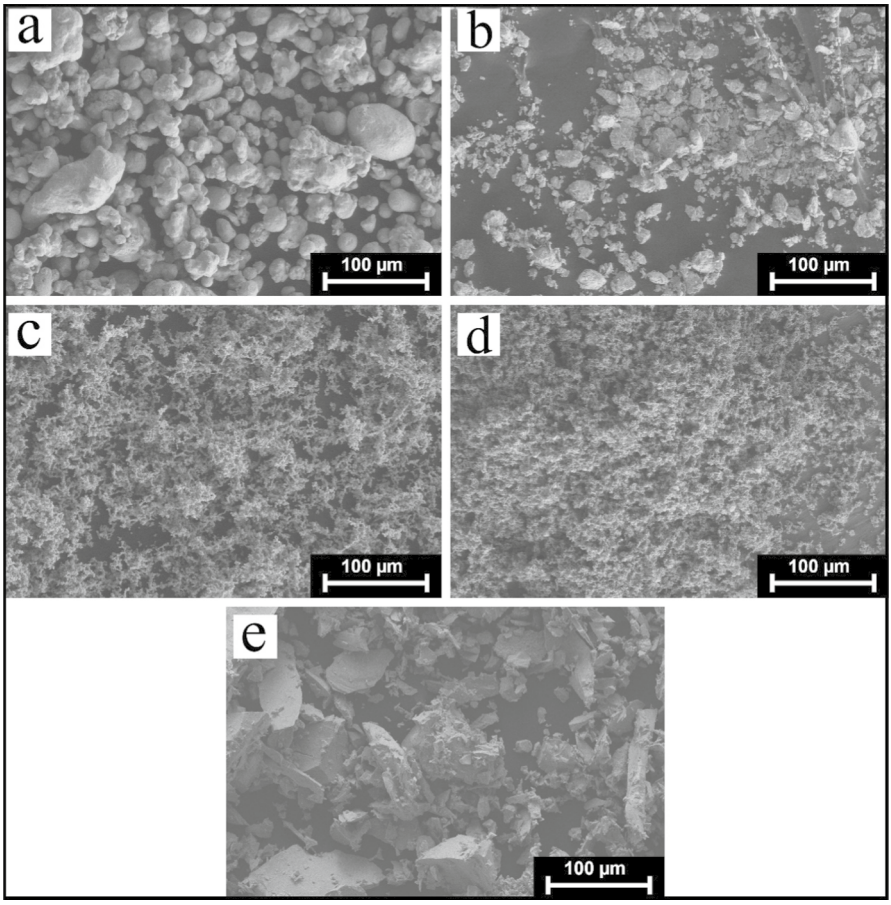


Fig. 1 SEM images of the initial particles used for the produce of HEA particles; **a** Fe, **b** Cr, **c** Ni, **d** Co and **e** Mn

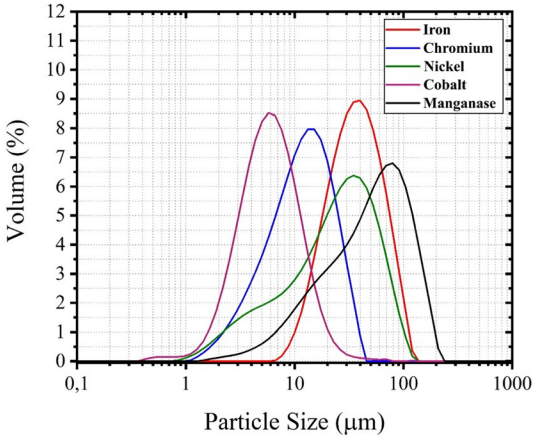


Fig. 2 Particle size distribution curves of the initial particles

addition, an interesting feature of nickel powders is their tendency to agglomerate. Figure 1d, e shows morphology of the Co and Mn particles, respectively. As can be seen in Fig. 1d, the Co particles have irregular morphology, and it is determined that the particle size distribution is relatively narrow. The particle morphology of Mn powders was determined as irregular and sharp-edged particle (Fig. 1e). In addition, the particle size distribution of the Mn particles ranges from approximately 10 to 120 µm. When examining the particle size distribution curves (Fig. 2), the particle size distributions are found to be compatible with the SEM images. The average particle size of the initial particles (Fe, Cr, Ni, Co, Mn) is shown in Table 4.

Morphological images and EDS analyses of HEA particles produced for different milling times are shown in Fig. 3. As can be seen in Fig. 3, the ball milling process directly affects the particle morphology [25, 26, 38, 39]. Since the mechanical alloying process took place in the ball milling environment, the particle morphologies begin to change and five different alloying elements begin to form composites with each other after 0.5 h of milling. As seen at the end of 0.5 and 5 h of milling, it is understood that particle morphology gradually differentiates with increasing milling time, and particles with different morphologies begin to form an integrated particle with a single morphology due to ball-powder-ball deformation. This situation is inherent in the mechanical alloying process, which includes mechanisms such as cold welding and fracture [40].

The most important result observed before the 1 h of milling is that all the powders are crushed and as a result, very fine HEA alloy powders are obtained. There can be two main reasons for obtaining fine HEA alloy powders as a result of a short milling process. The first of these can be the extraordinary fracture behavior observed in short milling times using liquid process control agent, as observed in other studies [41, 42]. The second reason can be the contribution of hard particles to the milling process by cutting effect [43, 44] until they break. However, there is a small amount of flake-like HEA alloy powders within the powder mass at the end of the 1 h of milling. Cold welding is a phenomenon caused by the deformation mechanism in mechanical alloying processes. Deformation mechanisms occurring between balls, jars and particles can cause many different phenomena such as cold welding, fracture, agglomeration and flattening. For the cold welding mechanism to take place, it is important to have metal-to-metal contact. Therefore, cold welding is more likely to occur in metals that have been cleaned of possible oxide layers on the surface after fracture. In addition,

Table 4 Average particle size of initial particles

Particle	Average particle size (µm)
Fe	38.52
Mn	56.62
Cr	12.54
Ni	26.04
Co	6.36

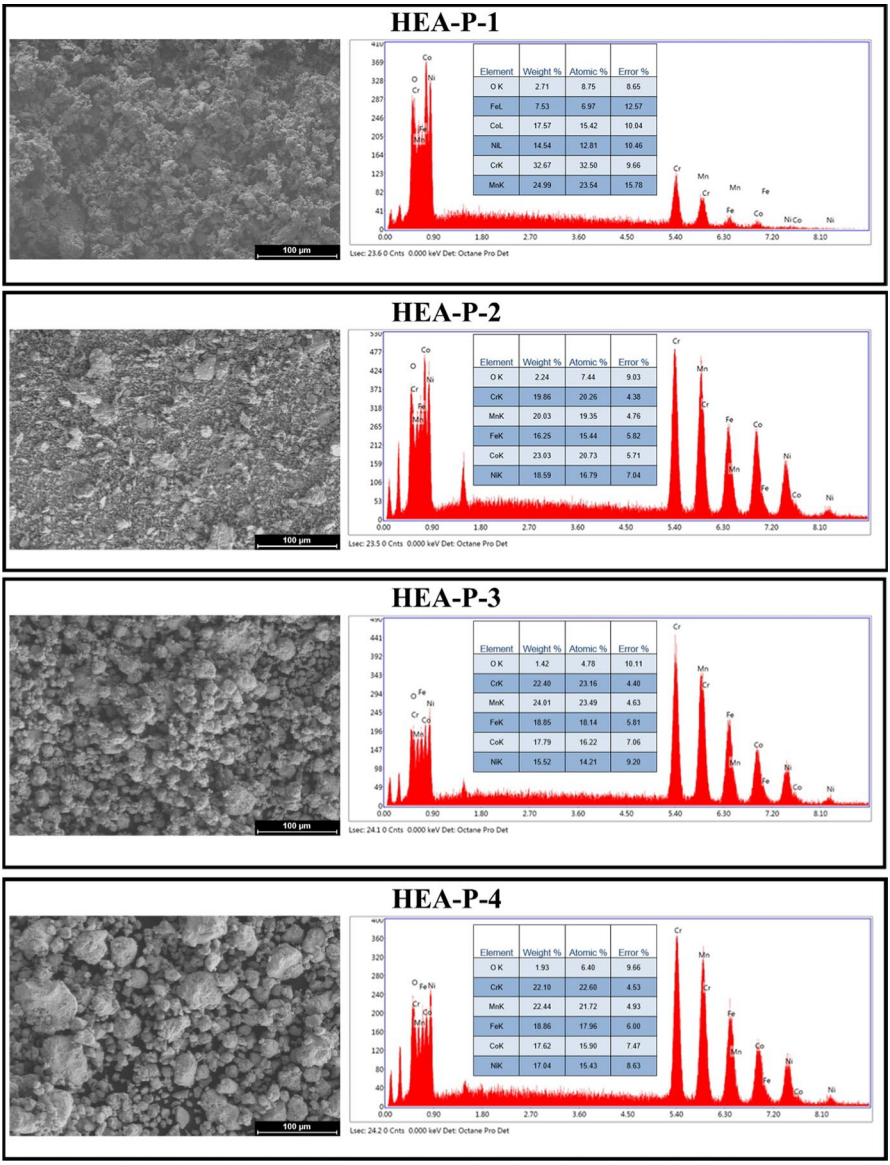


Fig. 3 SEM and EDS images of HEA particles produced with different milling times

new phases can be formed during mechanical alloying due to phase transformation, which increases the probability of cold welding by increasing atomic bonds [45]. After 1 h of milling, the cold welding process was reactivated, as can be seen at the end of 3 and 5 h of milling. This result can be attributed to the repeated fracture-cold welding cycle until the powders reach the critical deformation level during the mechanical alloying. In addition, the increasing temperature

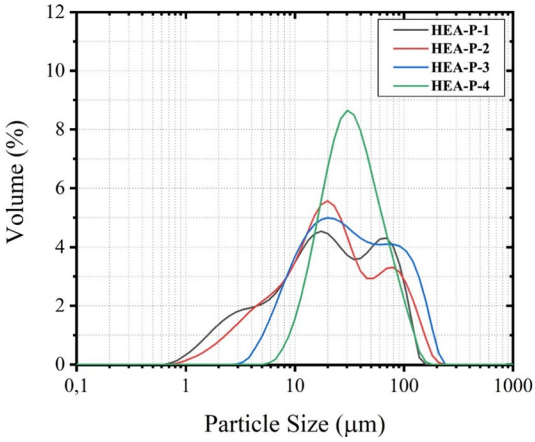


Fig. 4 Particle size distribution graph of the HEA particles produced with different milling times

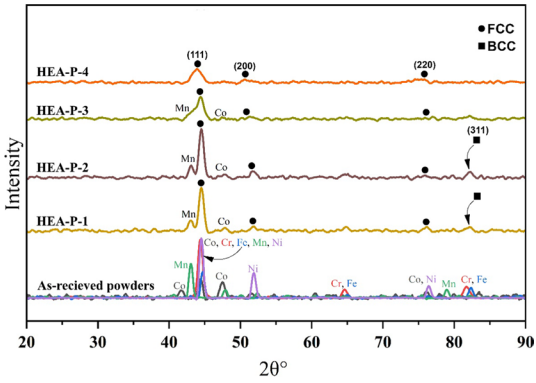


Fig. 5 XRD patterns of as-received and equal weight mixed CoCrFeMnNi powders with increasing milling time

due to increasing deformations can be cause the clumping of the particles. When the cold welding level is compared, a more intense cold welding is observed in the powders obtained after 5 h of milling. Therefore, the powder sizes obtained after 5 h of milling are higher. When the EDS spectrum results are examined, it is seen that the nanocrystals of all HEA powder produced by mechanical alloying exhibit a homogeneous structure in their composition. The homogeneous distribution of the milled powders is a big gain in terms of milling time. It is seen that it has a similar mixing ratio when longer milling times (1–3–5 h) are taken into account. Particle size distribution curves of HEA particles obtained after mechanical alloying are shown in Fig. 4. As can be seen in Fig. 4, the particle size distribution obtained after 5 h of milling is single peaked and has a relatively narrow distribution range.

The XRD graph of as-received and equal weight mixed CoCrFeMnNi powders with increasing milling time is presented in Fig. 5. XRD graphs of powders (as-received powders) that were not subjected to mechanical alloying process were handled one by one and plotted on a single graph. In this graph, each Co–Cr–Fe–Mn–Ni

powder is marked in a different color. The intensity of the FCC and BCC phases increases in parallel with the mechanical alloying time. The mechanical alloying time of the CoCrFeMnNi alloy corresponds to the BCC phase rich in Fe–Cr, and Ni corresponds to the FCC phase. As the milling time increases, the BCC peaks corresponding to Fe–Cr decrease and continue to dissolve in the Ni-based FCC matrix. After 3 h of milling, a single-phase FCC phase structure was obtained. Mn and Co elemental peaks are observed at times up to 0.5, 1 and 3 h of milling, respectively. The Mn and Co peaks continued to decrease with the increase in the mechanical alloying time. Co is the last element that dissolves completely after mechanical alloying. The FCC phase density increased with the increase in milling time and became the main phase after 5 h of milling (HEA-P-4).

Thermogravimetric analysis results of HEA powders prepared at different milling times are shown in Fig. 6. When Fig. 6 is examined, it is clearly understood that oxidation resistance increases with increasing milling time. When only 0.5 h (mass change nearly 18 wt%) and 1 h (mass change nearly 24 wt%) of alloying are compared, the oxidation resistance of the particles obtained after 0.5 h seems to be higher (HEA-P-1). It is thought that the absence of HEA in the structure and the smaller size of the particles obtained after 1 h cause a decrease in oxidation resistance (HEA-P-2). However, as HEA started to form with increasing milling time, it is understood that the mass increase dramatically decreased and so the oxidation resistance increased. A significant increase in oxidation resistance was observed with the formation of the HEA phase structure (HEA-3 and HEA-4). This confirms the stability and superior properties of HEA at high temperatures. It should be noted that with increasing milling time, a transition from five different metal powder structures to HEA powder structure was achieved, and the oxidation resistance feature of this new alloy powder structure was observed. The fact that HEAs are alternative materials used in applications at high temperatures which shows that they have high oxidation resistance [46]. Therefore, according to XRD results (Fig. 5), it is normal for HEA particles fabricated with 3 h (mass change nearly 7 wt%) and 5 h (mass

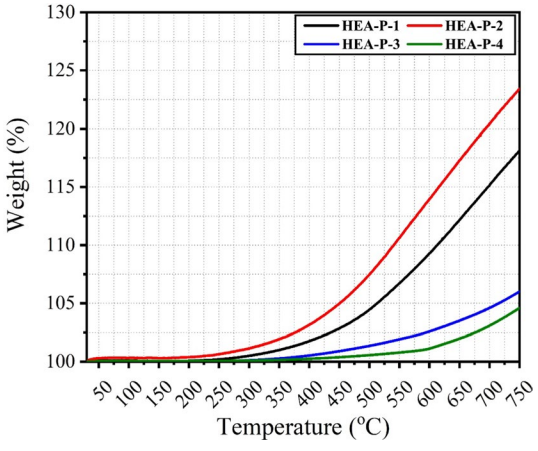


Fig. 6 Thermogravimetric analysis result of the HEA powders produced by mechanical alloying process with different times

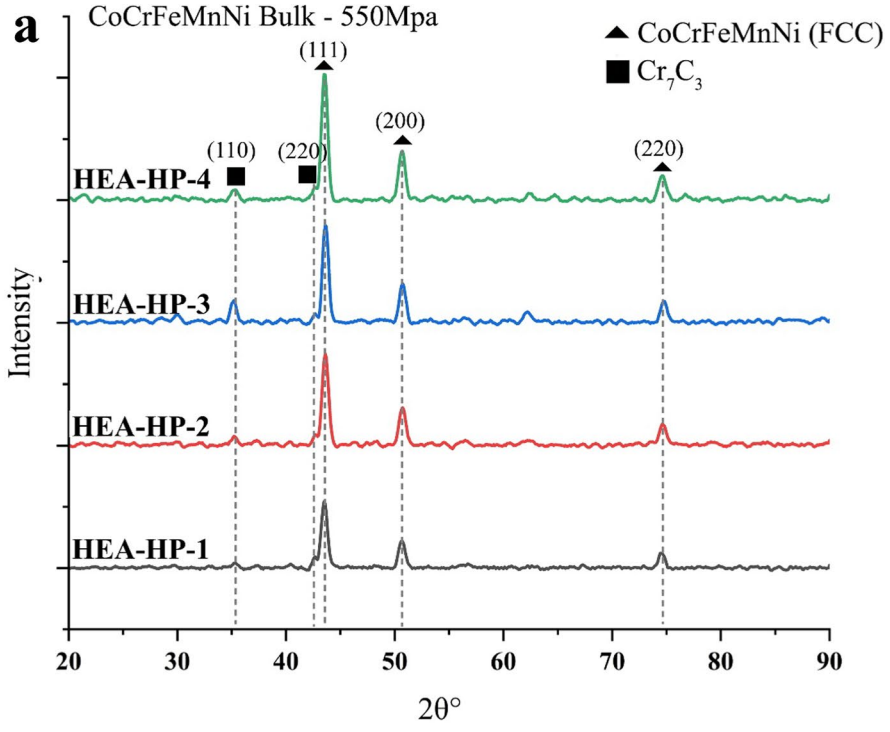
Fig. 7 XRD patterns of bulk samples; **a** hot-pressed at 550 MPa and sintering 1000℃, **b** hot-pressed at ▶ 650 MPa and sintering 1000℃

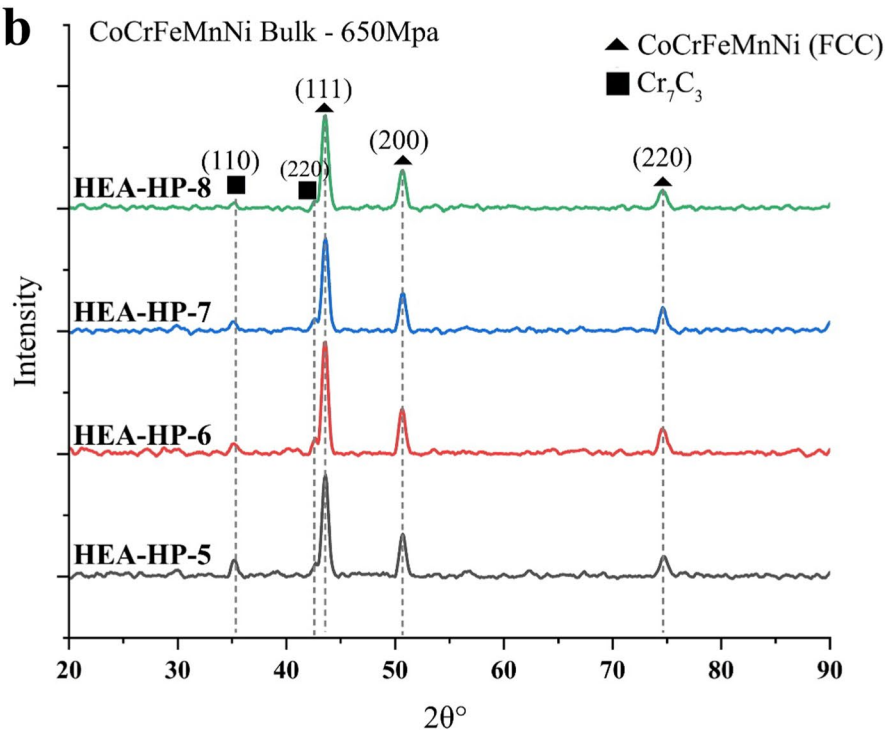
change nearly 5 wt%) of milling (HEA-P-3 and HEA-P-4) to have a very high oxidation resistance compared to particles fabricated at short milling times.

Structural Properties of Bulk Materials

XRD graphs of bulk samples are presented in Fig. 7. When the graph is examined, no significant change was observed in the XRD peaks with the change in hot-pressing pressure. In all sintered sample groups, CoCrFeMnNi peaks with FCC structure are observed dominantly. Cr_7C_3 formation also occurred during sintering. Cr_7C_3 phase formation is quite common after sintering and heat treatment of CoCrFeMnNi HEAs [32, 47–51]. However, since there is a very small amount of Cr_7C_3 formation, its effect on the mechanical and chemical properties of the structure is thought to be very low. It is considered that C contamination comes from the graphite lubricant used to reduce friction on the mold inner walls during hot pressing. Due to [37] the release of internal stresses by thermal activation during the sintering process, an increase in peak density was observed after processing. At the same time, no impurity phase was found after sintering process.

Figures 8 and 9 show microstructure images of the HEA. The HEA had a totally dense microstructure with brilliant and dark gray grains, as illustrated in Fig. 8a. The pores at the grain boundaries, which are highly visible in the sample pressed at 550 MPa, indicate that the pressure is insufficient for sample compression. It should not be overlooked that the existence of these voids and pores is affected by the milling times as well as the applied pressing pressure. Although the density increases with increasing milling time, the presence of pore-like structures in Fig. 8c can be attributed to two reasons. Firstly, when the microstructures of HEA samples produced using powders obtained by 0.5 and 1 h milling are examined, it is observed that there is a good degree of densification. As seen in the powder size distributions (Fig. 4), it is understood that the powder size shows a bimodal distribution in these two milling times. It has been observed that the presence of two distributed powder sizes within the powder mass plays an effective role in closing the porosity during densification. The microstructure of the samples produced using powders milled for 3 and 5 h is different from the powders milled for 0.5 and 1 h. If you pay attention, the bimodal distribution started to deteriorate after 3 h of milling time (Fig. 4). However, there is a small amount of powder in the structure that deviates from the average particle size. In this stage, cold welding is dominant process. As seen in Fig. 8c, cold-welded powders are larger in size and present in the microstructure. Other powders got in between these large-sized powders and prevented the grain boundary contact of the cold-welded structure with each other. Although the density increases with increasing milling time, this is thought to be the reason for the presence of pore-like structures in the microstructure, as seen in Fig. 8c. Secondly, overetching may also have caused this situation. In Fig. 8d, as a result of 5 h milling, all of the powders became cold-welded and turned into a hemispherical morphology.


a
CoCrFeMnNi Bulk - 550Mpa
CoCrFeMnNi (FCC)
Cr7C3
(111)
(200)
(110)
(220)
(220)
HEA-HP-4
HEA-HP-3
HEA-HP-2
HEA-HP-1
Intensity
20
30
40
50
60
70
80
90
2θ°


b
CoCrFeMnNi Bulk - 650Mpa
CoCrFeMnNi (FCC)
Cr7C3
(111)
(200)
(110)
(220)
(220)
HEA-HP-8
HEA-HP-7
HEA-HP-6
HEA-HP-5
Intensity
20
30
40
50
60
70
80
90
2θ°

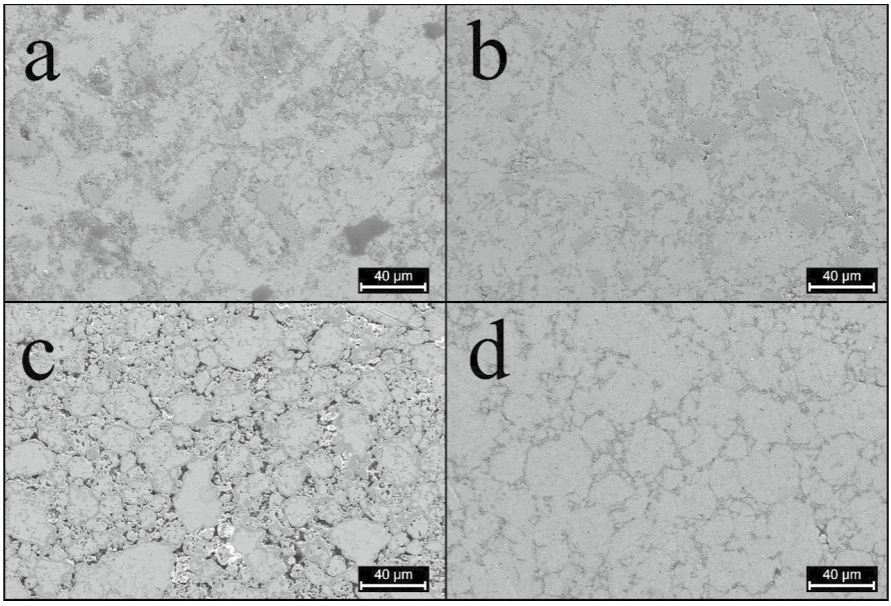


Fig. 8 Microstructure images of hot-pressed samples at 550 MPa; **a** HEA-HP-1, **b** HEA-HP-2, **c** HEA-HP-3, **d** HEA-HP-4

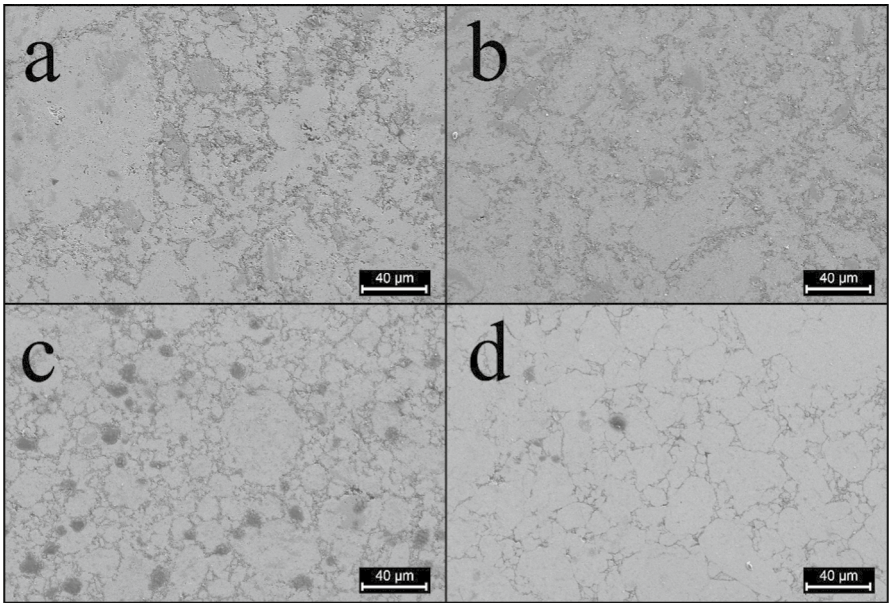


Fig. 9 Microstructure images of hot-pressed samples at 650 MPa; **a** HEA-HP-5, **b** HEA-HP-6, **c** HEA-HP-7, **d** HEA-HP-8

Therefore, as seen in Fig. 8d, a structure with homogeneous grain size and no porosity was obtained. This situation is seen similarly in the samples applied to 650 MPa pressure.

As can be seen in Fig. 9, although the sintering temperature remained constant, the increase in the hot-pressing pressure in the pretreatment position contributed significantly to the densification of the HEA particles and the pore amount decreased significantly. It should be noted that due to this positive effect of the hot-pressing pressure, the pores between the grain boundaries seen in Fig. 8 have completely disappeared in Fig. 9. This is clearly seen in the samples obtained with 3 h milling times as seen in the microstructure images in Figs. 8c and 9c. Another important result obtained from the microstructure images in Figs. 8 and 9 is that the microstructures obtained by hot-pressing the powders subjected to the 5 h of milling (HEA-HP-4 and HEA-HP-8), in which the best homogeneous powder size are obtained, are also the most homogeneous microstructure. As a result, microstructures with high homogeneity and low pore amount were obtained by increasing the milling time applied in the hot-pressing process.

Density and Hardness Results

The relative density changes in the bulk samples fabricated with different milling times and hot-pressing pressures is presented in Fig. 10. When Fig. 10 is examined, it was observed that the density in the samples increased with increasing pressure and milling time. It was found that the sample produced with 5 h of milling and at 650 MPa pressure (HEA-HP-8) has the highest relative density with 86.29%, while the sample fabricated with 0.5 h of milling and 550 MPa pressure (HEA-HP-1) shows the lowest relative density with 77.34%. In the hot-pressing process performed at 550 MPa pressure, the relative density increased by 8.6% as the milling

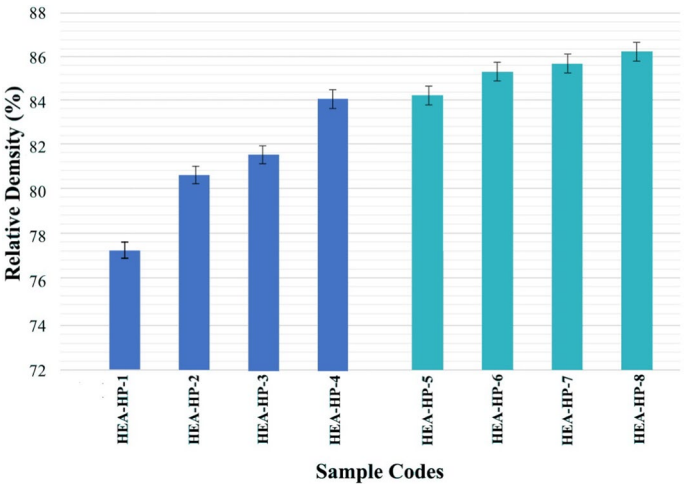


Fig. 10 Relative densities of hot-pressed and sintered CoCrFeMnNi samples

time increased from 0.5 to 5 h. This situation is lower in the hot-pressing process performed at 650 MPa pressure, and the relative density increased by 2.5% as the milling time increased from 0.5 to 5 h. With the effect of the high pressure applied during the densification process, the powders are pushed into the gaps and the gaps of the powders are filled, thus increasing the density. It was determined as a result of the tests that the density of the samples with a compression pressure of 650 MPa was higher than the samples with a compression pressure of 550 MPa. It should be noted that the morphological changes, fracture and cold welding events observed with increasing milling time change the densification behavior of the powder mass. The result of higher density values being obtained with increasing milling time can be attributed to the presence of cold-welded powders and fractured powders within the powder mass. With increasing milling time, the amount of small-size powder within the powder mass increases, and this ensures easy filling of the pores of small-size particles during pressing. Density values showed a significant increase with increasing hot-pressing pressure as well as an increase in the milling time.

The hardness values of the bulk samples are given in Fig. 11. When Fig. 11 is examined, it should be noted that the materials with the highest density also have the highest hardness value. The highest hardness value was measured as 263 Brinell, and this hardness value was obtained in the samples produced by hot-pressing of 5 h milled powders at 650 MPa and then sintering at 1000 °C for 2 h (HEA-HP-8). On the contrary, the lowest hardness value was measured as 144 Brinell hardness, and this hardness value was obtained in the samples produced by hot-pressing of 0.5 h milled powders at 550 MPa and then sintering at 1000 °C for 2 h (HEA-HP-1). In the hot-pressing process performed at 550 MPa pressure, the hardness increased by 80% as the milling time increased from 0.5 to 5 h. This situation is lower in the hot-pressing process performed at 650 MPa pressure, and the hardness increased by 26% as the milling time increased from 0.5 to 5 h.

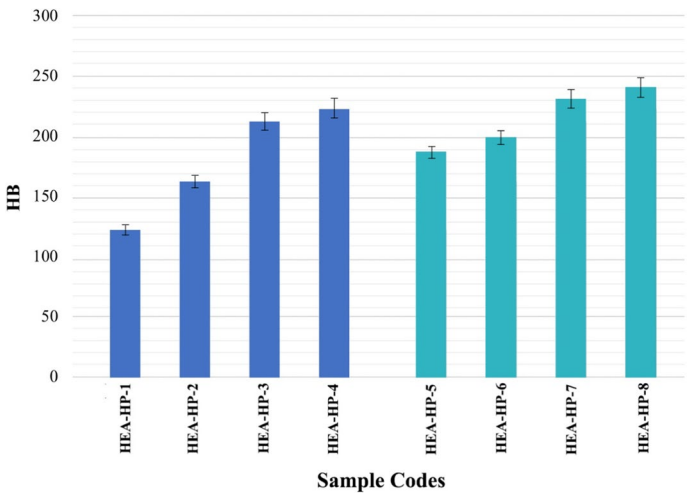


Fig. 11 Brinell hardness of hot-pressed and sintered CoCrFeMnNi samples

When microstructure images, relative density and hardness values were examined as a whole, denser samples have a more regular and more homogeneous structure. Increasing hot-pressing pressure created a denser structure and provided higher hardness values. This observation clearly demonstrates that there is a direct relationship between relative density and hardness. Cr has a high tendency to form carbides and oxides. As the milling time progressed, especially during the 5 h milling period, the Cr_7C_3 phase was observed in the structure. This is due to the presence of Cr, which is highly susceptible to reacting with C. It is considered that C contamination comes from the graphite lubricant used to reduce friction on the mold inner walls during hot pressing. In addition, the increase in the Cr_7C_3 phase formed in the structure after sintering is another factor in increasing the hardness of bulk samples.

Wear Test Results

The coefficient of friction (COF) results are given in Fig. 12. In Table 5, the surface roughness values of the samples are presented. It is seen that the surface roughness value (Ra) decreases as compression pressure and the milling time increases. The decrease in surface roughness values with increasing milling time can be attributed to the decreasing particle size and homogeneous particle size distribution due to increasing milling time.

In order to eliminate the effect of surface roughness values on the wear performance of the alloy, the surface roughness values of all samples were equalized to be approximately 0.15 μm before the wear tests. Figure 12 shows that the sample with the lowest average friction coefficient was the sample fabricated at 650 MPa compression pressure and 5 h of milling (HEA-HP-8), and its COF value was 0.28. The sample with the highest average friction coefficient was determined as 1.03 for the sample fabricated at 550 MPa compression pressure and 0.5 h of milling (HEA-HP-1). It has been observed that these COF values are compatible with the literature [52–54]. It is thought that the reason for the increase in the friction coefficient in the 180th second of the wear time which was subjected to 550 MPa and 5 h of milling (HEA-HP-1) was caused by accumulation of wear debris due to wear.

The wear rate graphs of the bulk samples are presented in Fig. 13. According to the results, it was observed that the wear rate values decreased with increasing milling time for both pressure values. Because the increase in the milling time both increased the density and the hardness values of the samples. The lowest wear rate was obtained in the sample produced with 5 h of milling and at 650 MPa (HEA-HP-8). This sample also represents the parameter in which the highest value of hardness and density is obtained. When HEA-HP-1 and HEA-HP-4 are compared, approximately 71.1% decrease in wear rate, and when HEA-HP-5 and HEA-HP-8 are compared, approximately 66.2% decrease in wear rate occurred depending on the increase in milling time. For the milling time of 5 h, where the highest wear resistance was obtained for both pressure values, the wear rate of the sample that was hot-pressed at 650 MPa (HEA-HP-8) was 94.1% lower than the sample that was hot-pressed at 550 MPa (HEA-HP-4). This result shows that an increase of 100 MPa in hot-pressing has a great effect on improving the wear resistance of the alloy.

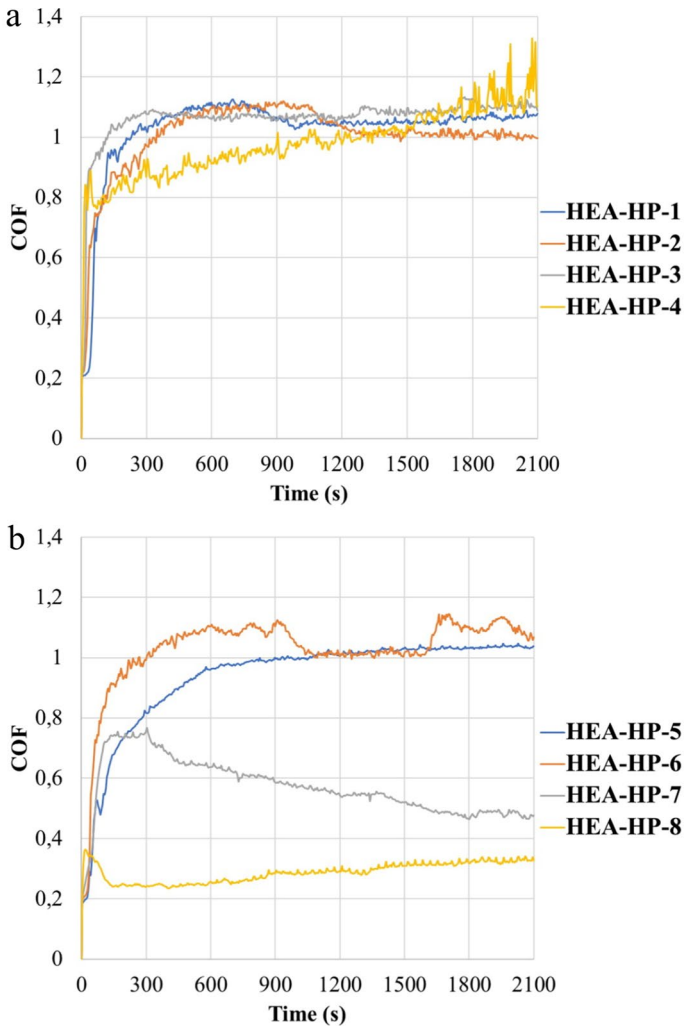


Fig. 12 COF graphs of bulk samples; **a** hot-pressed at 550 MPa, **b** hot-pressed at 650 Mpa

Table 5 Surface roughness values of bulk samples

Samples	Ra (μm)
HEA-HP-1	0.057
HEA-HP-1	0.039
HEA-HP-3	0.035
HEA-HP-4	0.021
HEA-HP-5	0.055
HEA-HP-6	0.046
HEA-HP-7	0.038
HEA-HP-8	0.022

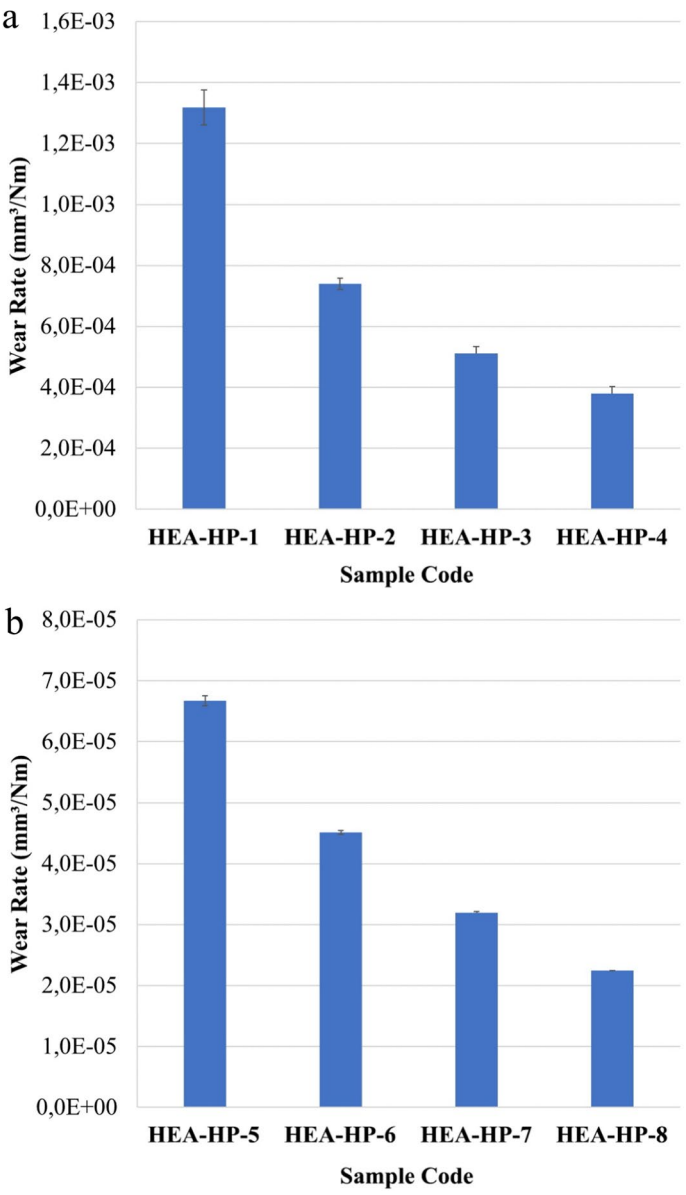


Fig. 13 Wear rates of bulk samples; **a** hot-pressed at 550 MPa, **b** hot-pressed at 650 MPa

Optical microscope, SEM and 3D profilometer images of the wear traces of the samples produced at different milling times and 550 MPa hot-pressing pressure are given in Figs. 14 and 15. When the optical images of wear trace were examined, it was observed that the wear trace width decreased with increasing milling time. The minimum wear rate and the lowest wear trace width were observed in samples

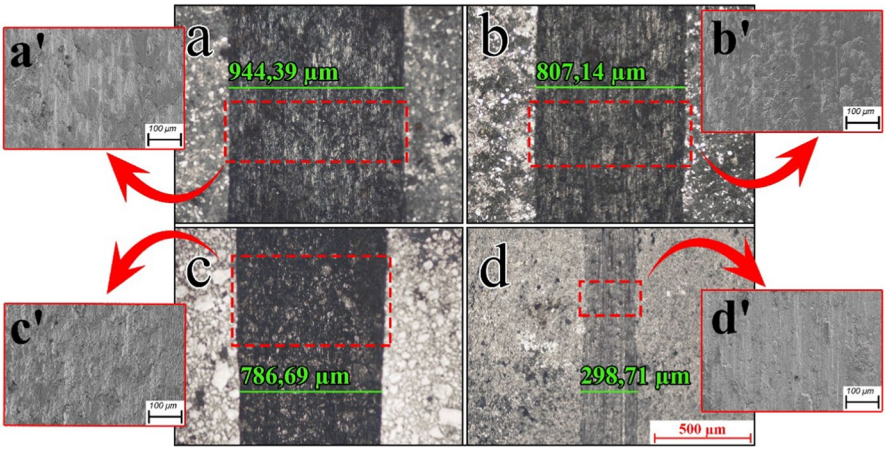


Fig. 14 SEM and optical microscope images of wear traces of the samples hot-pressed at 550 MPa; **a**–**a**' HEA-HP-1, **b**–**b**' HEA-HP-2, **c**–**c**' HEA-HP-3, **d**–**d**' HEA-HP-4

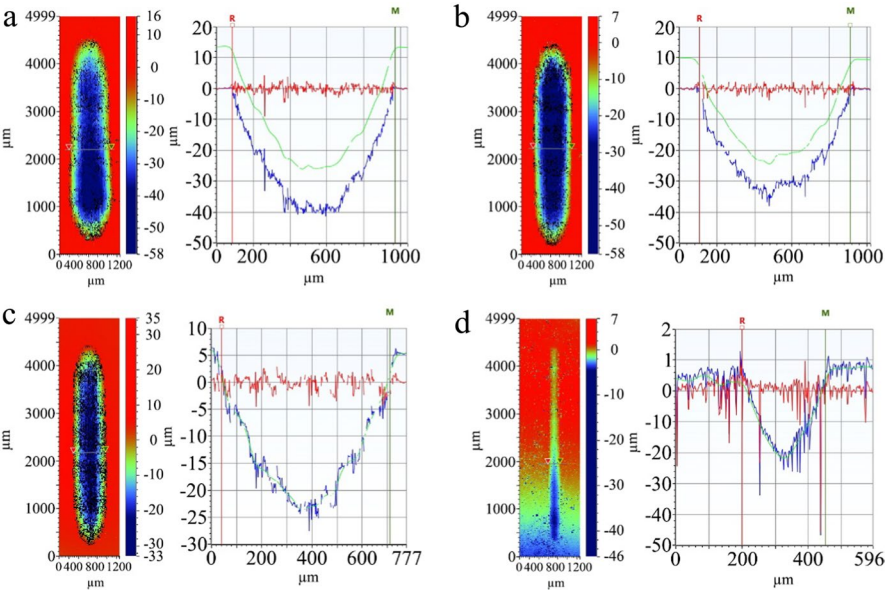


Fig. 15. Three-dimensional profilometer images of wear traces of the samples hot-pressed at 550 MPa; **a** HEA-HP-1, **b** HEA-HP-2, **c** HEA-HP-3, **d** HEA-HP-4

produced by hot-pressing of 5 h milled powders at the 550 MPa and then sintering at 1000 °C for 2 h (HEA-HP-4), which obtained the highest hardness and density value (Fig. 14). The highest wear trace width was found in the sample subjected to milling for 0.5 h (HEA-HP-1). SEM images of the area marked in red in the wear trace optical microscope images are presented in a', b', c' and d'. When these

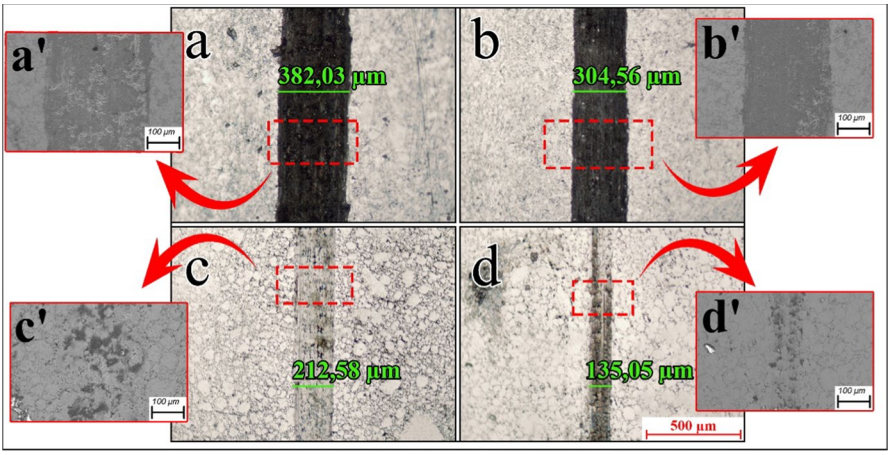


Fig. 16 SEM and optical microscope images of wear traces of the samples hot-pressed at 650 MPa; **a**–**a**' HEA-HP-5, **b**–**b**' HEA-HP-6, **c**–**c**' HEA-HP-7, **d**–**d**' HEA-HP-8

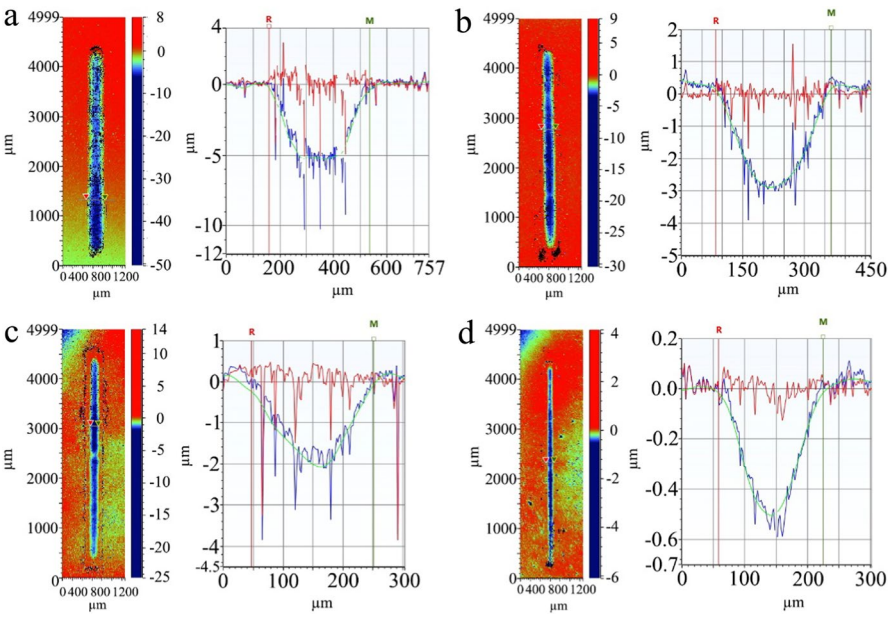


Fig. 17 Three-dimensional profilometer images of wear traces of the samples hot-pressed at 650 MPa; **a** HEA-HP-5, **b** HEA-HP-6, **c** HEA-HP-7, **d** HEA-HP-8

images were examined, it was determined that the wear mechanism was a combination of adhesive wear, abrasive wear and plastic deformation mechanisms. When the 3D profilometer images in Fig. 15 are examined, it is seen that the deepest wear trace belongs to the 0.5 h of milling (HEA-HP-1). It is also seen that the wear trace images obtained are compatible with the wear rate values.

Optical microscope, SEM and 3D profilometer images of the wear traces of the samples produced at different milling times and 650 MPa hot-pressing pressure are given in Figs. 16 and 17. When the wear trace optical images in Fig. 16 were examined, it was found that as the milling time increased, the wear trace width reduced. For the densification pressure of 650 MPa, the minimum wear rate and the lowest wear trace width and the highest hardness were observed in the sample, which was subjected to milling for 5 h (HEA-HP-8). The sample exposed to milling for 0.5 h had the greatest wear trace width (HEA-HP-5). The wear process was confirmed to be a combination of adhesive wear, abrasive wear, and plastic deformation mechanisms after these images were evaluated. When the 3D profilometer images in Fig. 17 are analyzed, it is clear that the sample milled for 0.5 h has the deepest wear trace (HEA-HP-5). The wear trace with the lowest depth was measured for the sample milled for 5 h (HEA-HP-8). When all images are evaluated together, it is clearly seen that both the milling time and the pressure value used in the hot-pressing have a great effect on increasing the wear performance of the alloy.

As the milling time progresses, the fine and hard particles such as Co, Cr and Ni in the powder material are coated or embedded with ductile iron particles. This helps to reduce the particle size and increase the percentage of solute atoms in the matrix. This increases the homogeneity and density of the bulk samples produced and improves wear and hardness properties. Also, as a result of grain refinement during milling, the proportion of grain boundaries increases, which inhibits the movement of dislocations, leading to an improvement in overall strength [24]. It has been reported that increasing the milling time leads to an increase in the solubility of Cr in the Cu matrix and a corresponding decrease in particle size, which improves mechanical properties [25, 39]. Therefore, the mechanical properties of the samples milled for a long time (3 and 5 h) were improved.

Conclusions

In the study, the effects of milling time and hot-pressing on the microstructure, density, hardness and wear resistance of CoCrFeMnNi alloys were studied. Also, the change of powder properties such as morphology, particle size, and oxidation resistance for different milling time was investigated in detail. The conclusions can be summarized as follows.

- After 1 h of milling, all the powders were ground and very fine CoCrFeMnNi HEA powders were obtained. The cold welding process was reactivated during the milling time of up to 3 h. After 5 h of milling, a more intense cold weld was observed in the powders obtained.
- After 3 h of milling, a single-phase FCC phase structure was obtained and became the main phase after 5 h of milling.
- As the milling time increased, hard and oxidation-resistant particles such as Co, Cr and Ni were embedded in the ductile Fe particles, which caused the oxidation resistance of the alloy to increase.

- The increase in hot-pressing pressure contributed to the densification of HEA particles and the number of pores decreased significantly. Microstructures obtained by hot-pressing of powders subjected to 5 h of milling are also the most homogeneous microstructures.
- The highest relative density was reached in HEA-HP-8 samples, while the lowest density was reached in HEA-HP-1 samples. The compressive force during densification increased the density by filling the gaps between the HEA powders. Additionally, the highest hardness value (263 Brinell) was obtained for HEA-HP-8 samples, where the highest relative density was obtained.
- The sample with the lowest average friction coefficient (0.28) and the lowest rate of wear was obtained for HEA-HP-8 samples. Observed wear mechanisms included plastic deformation, adhesion, and abrasive mechanisms.

Acknowledgements The authors would like to thank Scientific and Technological Research Council of Turkey (TÜBİTAK) for their financial support (Project number: 122M679). We would also like to thank the Higher Education Council of Turkey (YÖK) for providing scholarships to Tevfik Oğuzhan Ergüder within the scope of the 100/2000 program.

Author Contributions CB involved in investigation, writing—review and editing, and validation. FY involved in conceptualization, writing—review and editing, and supervision. TV involved in investigation, writing—review and editing, and validation. SBA involved in investigation, writing—review and editing, and validation. TOE involved in investigation, writing—review and editing, and validation.

Funding The study was supported by the Scientific and Technological Research Council of Turkey (TUBITAK) with project number 122M679.

Data Availability The data that support the findings of this study are available from the corresponding author.

Declarations

Conflict of interest The authors declare that they have no conflict of interest.

References

1. D. Yang, Y. Liu, H. Jiang, et al., *Journal of Alloys and Compounds* 823, 153729 (2020).
2. J.-W. Yeh, S.-J. Lin, T.-S. Chin, et al., *Metallurgical and Materials Transactions A* 35, 2533 (2004).
3. J. W. Yeh, S. K. Chen, S. J. Lin, et al., *Advanced Engineering Materials* 6, 299 (2004).
4. B. Cantor, I. T. H. Chang, P. Knight, and A. J. B. Vincent, *Materials Science and Engineering: A* 375–377, 213 (2004).
5. S. Ranganathan, *Current Science* 85, 1404 (2003).
6. Y. E. H. Jien-Wei, *Annales de Chimie: Science des Materiaux* 31, 633 (2006).
7. Y. Brif, M. Thomas, and I. Todd, *Scripta Materialia* 99, 93 (2015).
8. C. Stephan-Scherb, W. Schulz, M. Schneider, S. Karafiludis, and G. Laplanche, *Oxidation of Metals* 95, 105 (2021).
9. M. Dada, P. Popoola, and N. Mathe, *World Journal of Engineering* 20, 43 (2023).
10. Murty BS, Yeh J-W, Ranganathan S, Bhattacharjee PP *High-Entropy Alloys* (Elsevier, City, 2019).
11. Zhang C, Gao MC. *High-Entropy Alloys: Fundamentals and Applications* 399 (2016).
12. Zhang Y. *High-Entropy Materials*, Vol. 2 (Springer, 2019), p. 215.
13. G. Laplanche, U. F. Volkert, G. Eggeler, and E. P. George, *Alloy Oxidation of Metals* 85, 629 (2016).

14. S. Chen, Y. Tong, and P. K. Liaw, *Entropy* 20, 937 (2018).
15. Y. F. Ye, Q. Wang, J. Lu, C. T. Liu, and Y. Yang, *Materials Today* 19, 349 (2016).
16. D. B. Miracle and O. N. Senkov, *Acta Materialia* 122, 448 (2017).
17. N. Eißmann, B. Klöden, T. Weißgärber, and B. Kieback, *Powder Metallurgy* 60, 184 (2017).
18. A. Gali and E. P. George, *Intermetallics* 39, 74 (2013).
19. G. A. Salishchev, M. A. Tikhonovsky, D. G. Shaysultanov, et al., *Journal of Alloys and Compounds* 591, 11 (2014).
20. F. Otto, N. L. Hanold, and E. P. George, *Intermetallics* 54, 39 (2014).
21. F. Otto, A. Dlouhý, C. Somsen, H. Bei, G. Eggeler, and E. P. George, *Acta Materialia* 61, 5743 (2013).
22. B. S. Murty and S. Ranganathan, *International Materials Reviews* 43, 101 (1998).
23. M. C. Gao, J.-W. Yeh, P. K. Liaw, and Y. Zhang, *High-Entropy Alloys*, (Springer, Cham, 2016).
24. S. Chakraborty, A. K. Gupta, D. Roy, and Mallick A. Basu, *Materials Letters* 274, 128004 (2020).
25. S. Chakraborty, A. K. Gupta, D. Roy, and A. Basumallick, *Materials Letters* 257, 126739 (2019).
26. D. Roy, S. Chakraborty, A. K. Gupta, A. Basu Mallick, and C. C. Koch, *Materials Letters* 271, 127780 (2020).
27. D. Roy, S. Pal, C. S. Tiwary, A. K. Gupta, P. N. Babu, and R. Mitra, *Philosophical Magazine* 102, 189 (2022).
28. B. Gludovatz, A. Hohenwarter, D. Catoor, E. H. Chang, E. P. George, and R. O. Ritchie, *Science* 345, 1153 (2014).
29. J. Joseph, N. Haghdadi, M. Annasamy, et al., *Scripta Materialia* 186, 230 (2020).
30. F. Otto, An. Dlouhý, K. G. Pradeep, et al., *Acta Materialia* 112, 40 (2016).
31. Z. Li, K. G. Pradeep, Y. Deng, D. Raabe, and C. C. Tasan, *Nature* 534, 227 (2016).
32. C. Nagarjuna, K. Y. Jeong, Y. Lee, et al., *Advanced Powder Technology* 33, 103519 (2022).
33. D. Yim, M. J. Jang, J. W. Bae, et al., *Materials Chemistry and Physics* 210, 95 (2018).
34. C. D. Gómez-Esparza, R. Martínez-Sánchez, A. Duarte-Moller, and C. A. Rodríguez-González, *Microscopy and Microanalysis* 25, 2416 (2019).
35. Ł Rogal, D. Kalita, A. Tarasek, P. Bobrowski, and F. Czerwinski, *Journal of Alloys and Compounds* 708, 344 (2017).
36. W. Ji, W. Wang, H. Wang, et al., *Intermetallics* 56, 24 (2015).
37. S. H. Joo, H. Kato, M. J. Jang, et al., *Journal of Alloys and Compounds* 698, 591 (2017).
38. A. Bor, B. Jargalsaikhan, K. Uranchimeg, J. Lee, and H. Choi, *Powder Technology* 394, 181 (2021).
39. D. Roy, S. Chakraborty, A. K. Gupta, A. BasuMallick, R. O. Scattergood, and C. C. Koch, *Journal of Alloys and Compounds* 854, 157174 (2021).
40. C. Suryanarayana, E. Ivanov, and V. V. Boldyrev, *Materials Science and Engineering: A* 304–306, 151 (2001).
41. A. Canakci, S. Ozsahin, and T. Varol, *Powder Technology* 228, 26 (2012).
42. A. Canakci, F. H. Erdemir, T. Varol, R. Dalmış, and S. Ozkaya, *Powder Technology* 268, 110 (2014).
43. T. Varol and A. Canakci, *Powder Technology* 246, 462 (2013).
44. T. Varol, A. Canakci, and S. Ozsahin, *Journal of Alloys and Compounds* 739, 1005 (2018).
45. P. S. Gilman and J. S. Benjamin, *Annual review of materials science* 13, 279 (1983).
46. A. Ostovari Moghaddam, N. A. Shaburova, M. V. Sudarikov, S. N. Veselkov, O. V. Samoilova, and E. A. Trofimov, *Vacuum* 192, 110412 (2021).
47. M. Vaidya, A. Anupam, J. V. Bharadwaj, C. Srivastava, and B. S. Murty, *Journal of Alloys and Compounds* 791, 1114 (2019).
48. M. Vaidya, A. Karati, A. Marshal, K. G. Pradeep, and B. S. Murty, *Journal of Alloys and Compounds* 770, 1004 (2019).
49. Y. Xing, C. J. Li, Y. K. Mu, et al., *Journal of Materials Science & Technology* 132, 119 (2023).
50. R. Ravi and S. R. Bakshi, *Journal of Alloys and Compounds* 883, 160879 (2021).
51. M. Laurent-Brocq, P. A. Goujon, J. Monnier, et al., *Journal of Alloys and Compounds* 780, 856 (2019).
52. Z.-X. Wu, M.-J. He, C.-S. Feng, T.-L. Wang, M.-Z. Lin, and W.-B. Liao, *Journal of Thermal Spray Technology* 31, 1244 (2022).
53. M. Zhang, X. Zhang, M. Niu, Z. Jiang, H. Chen, and Y. Sun, *Tribology International* 174, 107736 (2022).
54. J. Joseph, N. Haghdadi, K. Shamlaye, P. Hodgson, M. Barnett, and D. Fabijanic, *Wear* 428–429, 32 (2019).

Publisher's Note Springer Nature remains neutral with regard to jurisdictional claims in published maps and institutional affiliations.

Springer Nature or its licensor (e.g. a society or other partner) holds exclusive rights to this article under a publishing agreement with the author(s) or other rightsholder(s); author self-archiving of the accepted manuscript version of this article is solely governed by the terms of such publishing agreement and applicable law.

Authors and Affiliations

Caner Bulut[1] · Fatih Yıldız[2] · Temel Varol[3,4] · Serhatcan Berk Akçay[3] · Tevfik Oğuzhan Ergüder[2]

✉ Caner Bulut
caner.bulut@igdir.edu.tr; caner.bulut86@erzurum.edu.tr

[1] Iğdır Technical Sciences Vocational School, Iğdır University, 76000 Iğdır, Turkey

[2] Department of Mechanical Engineering, Erzurum Technical University, 25050 Erzurum, Turkey

[3] Department of Metallurgical and Materials Engineering, Karadeniz Technical University, 61080 Trabzon, Turkey

[4] Medical Device Design and Production Application and Research Center, Karadeniz Technical University, 61080 Trabzon, Turkey